Structural Characterization of Boron-Containing Glassy and Semi-Crystalline Biosilicate by Multinuclear NMR

Henrik Bradtmüller,[a,b,&] Bianca M. Cerrutti,[b,&] Marina T. Souza,[c] Edgar D. Zanotto,[c] Hellmut Eckert[a,b,*]

[a]Institut für Physikalische Chemie, Westfälische Wilhelms-Universität Münster, Corrensstraße 30, D-48149 Münster, Germany.

[b]Instituto de Física de São Carlos, Universidade de São Paulo, CP 369, 13566-590, São Carlos, SP, Brasil.

[c]Universidade Federal de São Carlos, Departamento de Engenharia de Materiais, CP 676, 13565-905, São Carlos, SP, Brasil.

[&]equally contributing authors

*corresponding author: eckerth@uni-muenster.de

Abstract

In vitro, in vivo, and clinical studies - including histopathological, cytotoxicity, and genotoxicity analyses - over the past 25 years have proven the tremendous potential of the use of Biosilicate® as osteoinductive powders, scaffolds and even monolithic pieces. On the other hand, it is known that boron can influence vital processes such as embryogenesis, bone growth, and psychomotor skills, among others. Within continuing efforts to improve the properties of this bioactive material, in this article we explore the structural consequences of boron incorporating in small amounts and its effects on selected properties. Solid state ^{11}B NMR studies indicate that boron is likely present in the form of three-coordinate pyroborate units, with only minor fractions of four-coordinate species present. In contrast, ^{31}P MAS-NMR spectra reveal that phosphorus is almost exclusively present in the form of orthophosphate. The demand of the anionic borate network former for cationic charge compensation leads to an increase in average connectivity of the silicate network, as evident from ^{29}Si NMR. ^{31}P/^{11}B dipolar recoupling experiments indicate negligible amounts of borate–phosphate linkages in these glasses, presumably because of the low concentration of

each element. On the other hand, crystallization of the glassy biosilicate precursor produces crystalline $NaCaPO_4$ and $Na_2CaSi_2O_6$ as well as a residual amorphous material for which in addition no B-O-P linkages can be detected. Finally, we find that, surprisingly, in this particular glass, boron reduces the crystallization stability and has only a weak influence upon the tris-buffer solution dissolution kinetics.

Key words: bioactive, glass, boron, biosilicate, nuclear magnetic resonance, NMR

Introduction

Biosilicate® is a bioactive glass-ceramic having the composition 49.1 SiO_2 – 23.3 Na_2O – 25.8 CaO – 1.7 P_2O_5 (in mol%). Under controlled double-stage heat treatments, the glassy precursor material can be engineered to produce one or two crystalline phases: a sodium–calcium silicate ($Na_2CaSi_2O_6$) or both $Na_2CaSi_2O_6$ and a sodium–calcium phosphate ($NaCaPO_4$) phase, the so-called 2-phase BioSilicate. A large number *of in vitro, in vivo* and clinical studies, including histopathological, cytotoxicity, and genotoxicity studies, have proven its tremendous potential use as osteoinductive powders, scaffolds, and even monolithic pieces for bone, tissue and dental repair and healing [1,2]. Recent analyses have confirmed that Biosilicate® affects the osteoblast's expression of genes associated with the process of mineralization highlighting its osteostimulation property [3]. Within continuing efforts of improving the performance properties of this material even further, we have recently explored the incorporation of small amounts of boron into this material. Boron-doped bioactive glasses are currently attracting interest owing to increased bioactivity, improved biocompatibility and antibacterial function [4,5]. Boron can influence vital processes, including embryogenesis, bone growth and psychomotor skills [6,7]. To preserve bone health, a diet containing adequate amounts of boric acid enhances bone strength under compression [6]. It is also an essential mineral in the conversion of vitamin D to its active form. Finally, boron-containing bioactive materials induced increased proliferation of osteoblasts in cell cultures [6-8], and the controlled release of boron from bioactive glasses can favor the regeneration of bone tissues.

For developing boron-containing bioglass formulations with optimized performance, a detailed understanding of the structure/function relationship is required. To this end, X-ray diffraction and vibrational spectroscopic methods [8-11], as well as solid state NMR techniques have been applied [12-19]. Work by the Eden group stands out in particular reporting detailed compositional dependences and advanced connectivity information by two-dimensional dipolar NMR spectroscopy [12,13].

In the present contribution, we characterize the effect of the borate component upon the dissolution kinetics, and the structure of the biosilicate precursor glass, and the crystallized material 2-phase BioSilicate material using comprehensive multinuclear (^{31}P, ^{11}B, ^{23}Na, and ^{29}Si) magic-angle spinning (MAS) single- and double resonance NMR experiments.

Experimental

Sample preparation and characterization

Biosilicate precursor glasses $(SiO_2)_{0.49-x}(CaO)_{0.258}(Na_2O)_{0.233}(P_2O_5)_{0.017}(B_2O_3)_x$ (x = 0, 0.01 and 0.05) were obtained by melting adequate amounts of silica, $CaCO_3$, Na_2CO_3, B_2O_3, and Na_2HPO_4 for 3 h at 1350 °C, using a bottom-load furnace. Annealing with the objective of obtaining the glass-ceramic was done for 6 h at 425 °C. Glassy samples were characterized by differential scanning calorimetry, using a Netzsch 404 DSC instrument, operated at a heating rate of 10°C/min. Glass-ceramic phases were obtained by heat-treating the glassy samples under a controlled double-stage process, as described previously by Peitl et al. [20, 21]. Crystalline phases observed in the glass-ceramics were identified by X-ray powder diffraction, using a Rigaku Ultima IV diffractometer operated with a Cu-K_a source. Table 1 summarizes the glass compositions and their glass transition temperatures.

Bioactivity of the samples was tested in Simulated Body Fluid (SBF) as suggested in ISO 23317- [22] standard, and weight loss as a function of time was measured as indicated in ISO 10993-14 [23], exposing sample discs to 100 ml of TRIS buffer solution. Simultaneously, the pH of the solution was monitored over time (pH meter Hanna, H2211-01, USA).

NMR Studies

All reported NMR experiments were performed on a 5.7 T Varian 240-MR DD2, a 7.05 T Bruker DSX x and a 14.1 T Bruker Avance Neo spectrometer, using commercially available 2.5 and 4 mm double and triple resonance magic angle spinning (MAS) probes. ^{31}P MAS NMR spectra were recorded at 5.7 and 14.1 T, employing 90° pulses of 5 and 3 µs length, as well as MAS frequency of 5 and 10 kHz respectively for each magnetic flux density and a uniform recycle delay of 1200 s. Chemical shifts are reported relative to solid BPO_4 (^{31}P signal measured -29.3 ppm relative to a 85% H_3PO_4 solution). ^{29}Si MAS NMR spectra were recorded at 5.7 T, using 90° excitation pulses of 5 µs duration, 5.0 kHz MAS frequency and a recycle delay of 3600 s. Chemical shifts are reported relative to solid tetrakis(trimethylsilyl)silane (TTMSS) (measured -9.85 ppm relative to tetramethylsilane (TMS)).

^{11}B MAS NMR spectra were recorded at 5.7 and 14.1 T, using excitation pulses of 0.5 µs corresponding to a 30° flip angle and recycle delays of 30 s. Chemical shifts are reported relative to a BF_3·OEt solution, using crystalline BPO_4 (δ_{iso} = -3.5 ppm) as a secondary reference. ^{23}Na MAS NMR spectra were measured at 5.7 T, using excitation pulses of 1.0 µs corresponding to a 30° flip angle and a recycle delay of 1 s. Chemical shifts are reported

relative to a 1M aqueous NaCl solution, using crystalline NaCl (δ_{iso} = 7.2 ppm) as a secondary reference.

Data obtained from I = 1/2 nuclei (^{31}P and ^{29}Si) were deconvoluted into Gaussian components where possible. For the quadrupolar nuclei (^{11}B and ^{23}Na, I = 3/2) the DMFIT software [24] was used to simulate the spectra based on second-order perturbation theory.

Homonuclear ^{11}B-^{11}B dipole-dipole coupling strengths were determined by the static Hahn spin echo decay method [25]. A ^{11}B nutation frequency of 15 kHz was employed, corresponding to π-pulse durations of about 16.67 µs to guarantee selective excitation of the central $m = 1/2 \leftrightarrow m = -1/2$ Zeeman transition. The homonuclear dipolar second moments $M_{2(B-B)}$ were extracted from the Gaussian decay $I(2t_1)/I(0) = exp(-2M_2t_1^2)$ at short evolution times ($2t_1$ < 200 µs), by analyzing the slope of the semi logarithmic data representation ($\ln[I(2t_1)/I(0)]$ vs. $2t_1^2$).

^{11}B{^{31}P} rotational echo double resonance (REDOR) [26] experiments were carried out at 14.1 T, using the variant of Gullion and Schaefer [26,27], at a spinning speed of 15 kHz and nutation frequencies of 120 kHz for ^{11}B and 143 kHz for ^{31}P. 180° pulse lengths were 2.8 µs and 3.4 µs for trigonal ^{11}B and ^{31}P, respectively. Recycle delays of 1 s were used, optimized in respect to the relaxation of trigonal boron. Data were analyzed in terms of van Vleck average second-moment values $M_{2(B-P)}$, [28] which represent the mean squared average strengths of the respective spin couple's dipole-dipole coupling (^{11}B-^{31}P), using the parabolic approximation described in the literature [29].

^{31}P{^{11}B} rotational echo adiabatic passage double resonance (REAPDOR) [30] experiments were performed at 7.05 T under the following conditions: ^{11}B and ^{31}P nutation frequencies of 62.5 kHz, rotor frequency 15.0 kHz, and a ^{11}B adiabatic pulse of one-third of a rotor period. The recycle delays was 1000 s using a presaturation comb of 60 90° pulses.

Results and Discussion

Sample properties and Bioactivity

Table 1 summarizes the glass compositions and their physical properties, including glass transition temperatures, T_g, and crystallization temperatures, T_c. Surprisingly, Boron noticeably increases T_g, and decreases the crystallization temperature, thus reducing the overall thermal stability of these glasses (as inferred by T_c-T_g).

Table 1, Percentage of B_2O_3 in the glass (x), glass transition onset temperature T_g, crystallization onset temperature, T_x, and crystallization peak temperature, T_c, of bioactive glasses with compositions $(SiO_2)_{0.49-x}(CaO)_{0.258}(Na_2O)_{0.233}(P_2O_5)_{0.017}(B_2O_3)_x$. Estimated experimental error of ±2 °C.

x	T_g / °C	T_x / °C	T_c / °C
0.05	532	674	700
0.01	525	702	725
0.00	492	735	760

Figure 1 shows the dissolution data measured regarding weight losses upon exposure of discs of the bioactive material to 100 ml of TRIS solution. The data indicate that the dissolution characteristics of the materials are generally similar, with a tendency of the glassy materials to dissolve more rapidly and lead to larger pH changes than the crystallized samples. Furthermore, within both groups, the dissolution rates (and concomitant pH changes) tend to increase with increasing boron content (Fig. 1). However, regarding the materials bioactivity no significant change was observed, and all the samples presented the formation of hydroxycarbonate apatite (HCA) phase after being exposed to SBF solution for 16h, as expected and verified by FTIR tests (Figure 2). HCA main peaks can be observed for all samples in the FTIR spectra at 602 and 560 cm^{-1}.

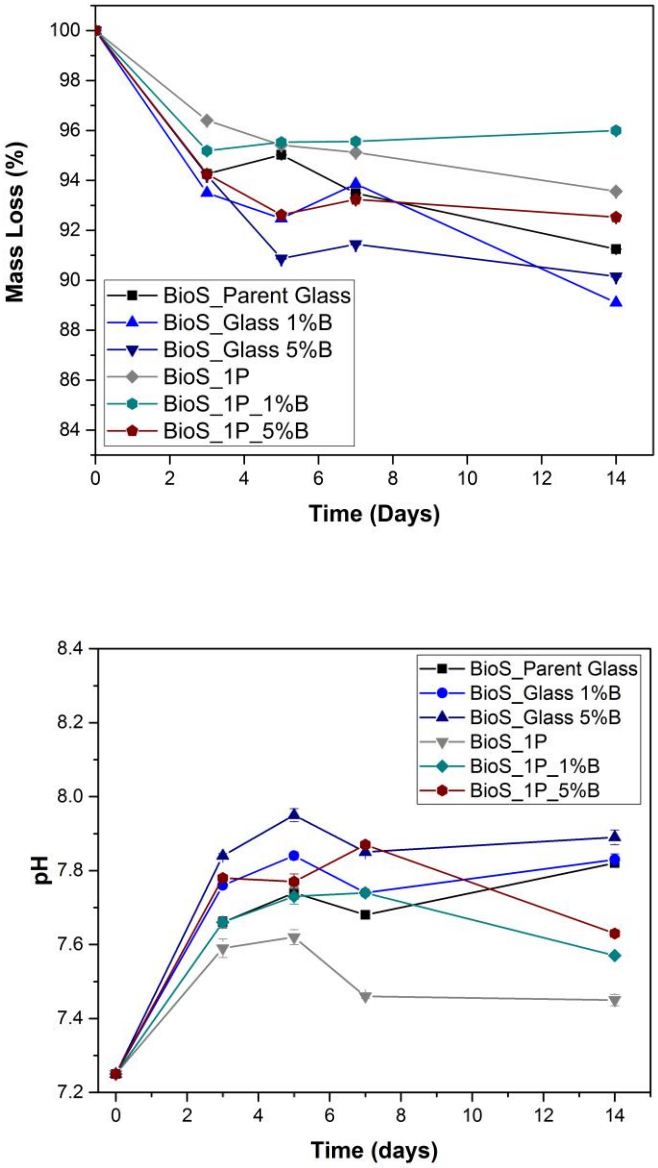

Figure 1: Temporal weight loss (top) and pH evolution (bottom) of B-containing amorphous and semi-crystalline Biosilicate samples (BioS) exposed to TRIS buffer solution.

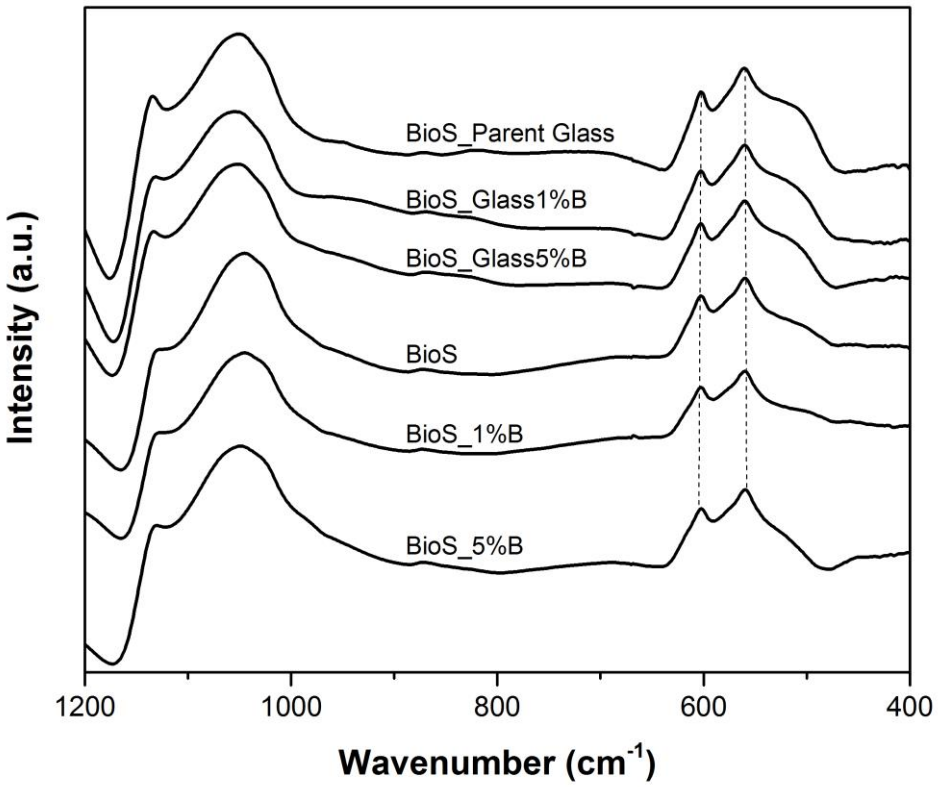

Figure 2: FTIR spectra for all samples after being exposed to SBF-K9 solution for 16 h. The formation of hydroxycarbonate apatite (HCA) was detected as expected for a bioactive material (main vibrational frequencies indicated by the black dashed lines), showing that boron incorporation did not significantly affect the high bioactivity of amorphous and semi-crystalline Biosilicate bioactivity.

Structural Studies on the Precursor glasses

Figure 3 shows the ^{29}Si MAS-NMR spectra of the three precursor glass samples. Asymmetric lineshapes are observed, whose average chemical shifts are given by -81.4 and -83.3 ppm, for the glasses having 1% and 5% boron, respectively. Table 2 summarizes the simplest possible deconvolution using two lineshape components near -80 and -90 ppm, corresponding to $Si^{(3)}$ and $Si^{(2)}$ sites, respectively. The fractional contribution of the $Si^{(3)}$ sites is significantly higher in the glass containing 5% boron, indicating that the incorporation of boron into biosilicate leads to an overall higher state of polymerization of the silicon species. Thus, the borate species competes successfully with silicate for network modifiers.

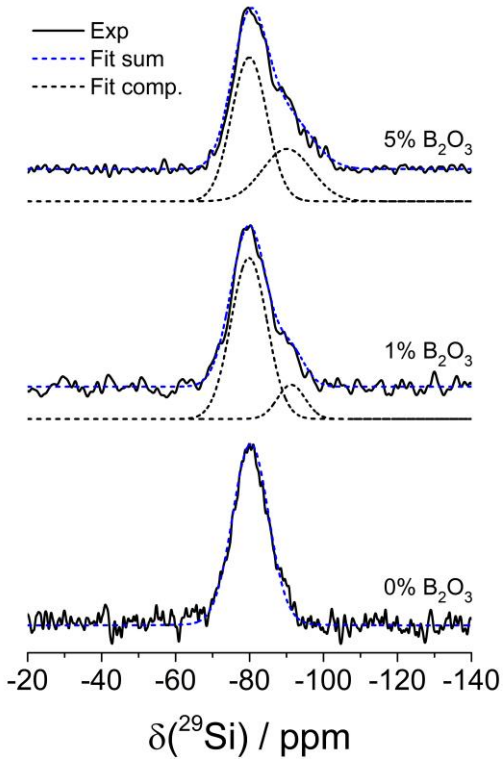

Figure 3: ^{29}Si MAS-NMR spectra of Biosilicate precursor glasses, containing 0, 1 and 5 mole% B_2O_3. Dashed curves denote the lineshape simulations based on the individual lineshape components depicted curves.

Table 2: ^{29}Si MAS-NMR parameters measured for the Biosilicate precursor glass.

x	δ_{iso} / ppm ± 0.5 ppm	*FWHM* / ppm ± 0.5 ppm	*F* / % ± 1%
0.00	-80.3	11.5	100
0.01	-79.8	11.5	86
	-91.3	8.7	14
0.05	-79.9	11.2	66
	-90.1	15.7	34

Figure 4 shows the ^{31}P MAS NMR spectra. The spectra are dominated by a broad Gaussian lineshape centered at 8.5 ppm, which can be attributed to fully depolymerized orthophosphate, $P^{(0)}$ species. Both samples also show a minor contribution near 1.0 ppm, corresponding to $P^{(1)}$ units (see Table 3). Within experimental error, the fractional areas do not depend on the B_2O_3 content. Furthermore, the constant chemical shifts observed for both components indicate that the distribution of Na^+ versus Ca^{2+} ions around the phosphate species is not influenced by the presence of borate.

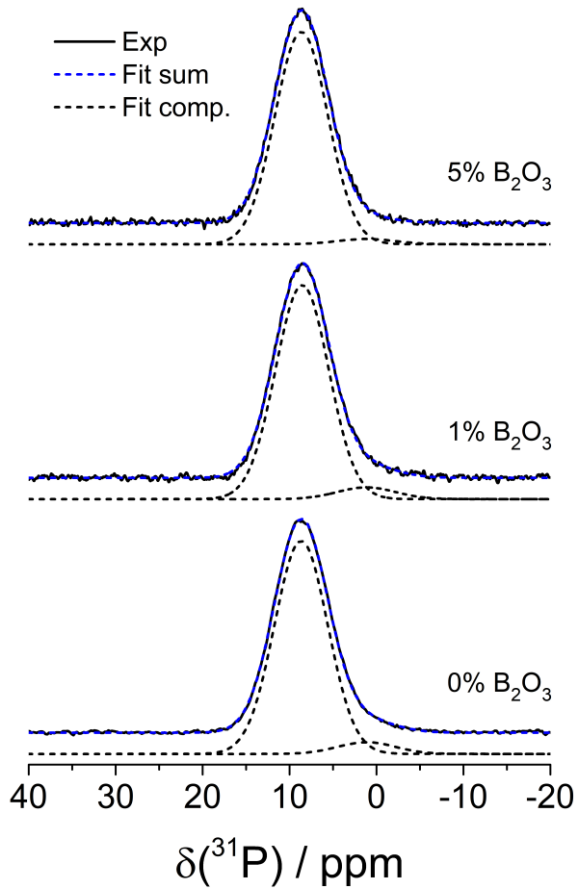

Figure 4: ^{31}P MAS-NMR spectra of Biosilicate precursor glasses, containing 1 and 5 mole% B_2O_3. Blue curves denote the lineshape simulations based on the individual lineshape components depicted as blue dashed curves.

Table 3: ^{31}P MAS-NMR parameters measured for the Biosilicate precursor glass.

x	**Species**	δ_{iso} **/ ppm ± 0.5 ppm**	***FWHM* / ppm ± 0.5 ppm**	***F* / % ± 2%**
0.00	$P^{(0)}_{0B}$	8.7	7.2	94
	$P^{(1)}_{0B}$	1.2	7.9	6
0.01	$P^{(0)}_{0B}$	8.6	7.2	94
	$P^{(1)}_{0B}$	1.2	7.9	6
0.05	$P^{(0)}_{0B}$	8.6	7.2	97
	$P^{(1)}_{0B}$	1.2	7.9	3

Figure 5 shows the field dependent ^{11}B MAS-NMR spectra and Table 4 summarizes the corresponding lineshape components. Two distinctly different components can be identified: the dominant one gives rise to a field-dependent MAS-NMR signal that reflects the result of nuclear electric quadrupolar interactions upon the Zeeman energy levels, as described by Second-order Perturbation Theory. The quadrupolar coupling constant C_Q near 2.55 ± 0.05 MHz and an electric field gradient asymmetry parameter of η_Q = 0.50 ± 0.05 are typical of three coordinated boron atoms bearing either one non-bridging and two bridging oxygen atoms (metaborate-type, $B^{(2)}$ units) or two non-bridging and one bridging oxygen atoms (pyroborate-type, $B^{(1)}$ units). The second component is represented by a simple

Gaussian line, reflecting rather weak quadrupolar interactions as typically observed for four-coordinated ($B^{(4)}$ species). The fraction of four-coordinated species, N_4, in the glass containing 1 mole % B_2O_3 is significantly lower than in the glass with 5 mole % B_2O_3. This finding is consistent with the behavior of binary alkali borate glasses with high modifier-to-boron ratios $R = [M_{(2)}O]/[B_2O_3]$, which indicate a decrease of N_4 with increasing R as R exceeds a value of 0.5 [31].

Table 4: ^{11}B MAS-NMR spectral fitting parameters of the glasses under study.

		B^{III}				B^{IV}		
x	***B*₀ / T**	**δ_{iso} / ppm**	**C_Q / MHz**	**η_Q**	***F* / %**	**δ_{iso} / ppm**	***FWHM* / ppm**	***F* / %**
		± 0.5 ppm	**± 0.1 MHz**		**± 1%**	**± 0.5 ppm**	**± 0.5 ppm**	**± 1%**
0.01	5.7	18.7	2.6	0.59	84	-1.0	2.5	16
	14.1	18.5	2.6	0.55	88	-0.7	1.7	12
0.05	5.7	19.0	2.6	0.55	74	-0.6	2.5	26
	14.1	17.9	2.4	0.55	72	-0.1	2.0	28

Unfortunately, the NMR parameters characterizing the three-coordinated boron sites do not offer a reliable distinction between meta- and pyroborate species. A decision between these two alternatives is possible, however, by considering the overall charge balance that needs to be maintained at the glass composition, according to:

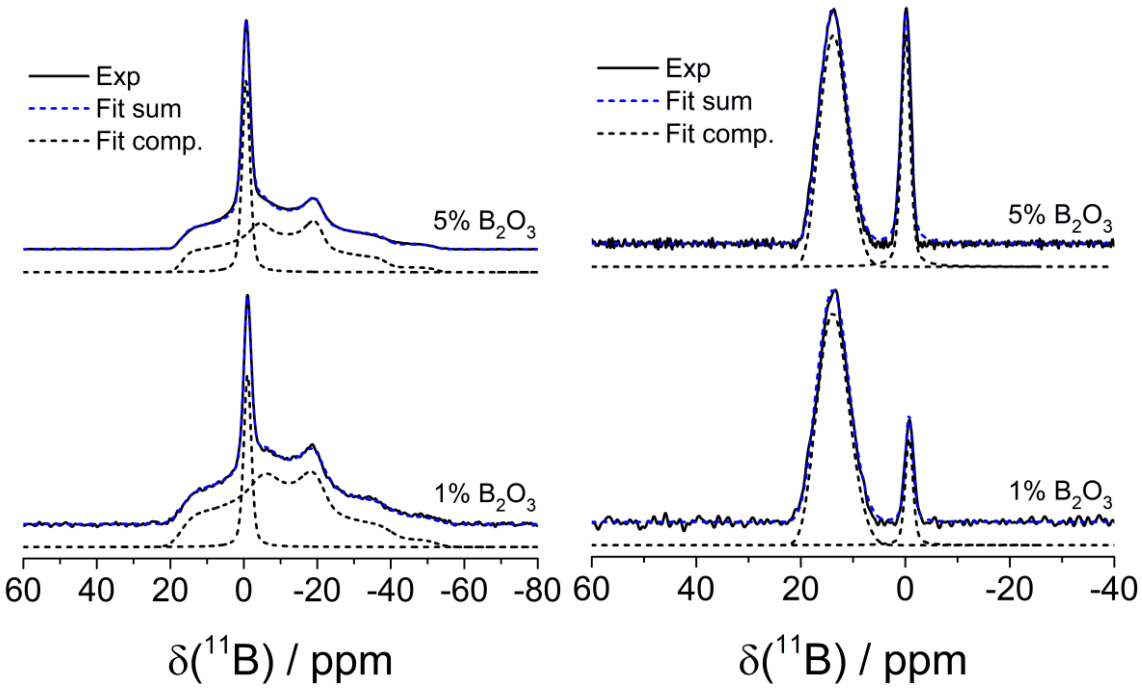

Figure 5: ^{11}B MAS-NMR spectra at 5.7 T (left) and at 14.1 T (right) of Biosilicate precursor glasses, containing 1 and 5 mole % B_2O_3. Blue curves denote the lineshape simulations based on the individual lineshape components depicted as dashed curves.

$$[Na^+] + 2[Ca^{2+}] = [Si^{(3)}] + 2\,[Si^{(2)}] + 3\,[P^{(0)}] + 2\,[P^{(1)}] + [B^{(4)}] + [B^{(2)}] + 2[B^{(1)}]$$

Here the square brackets denote the number of moles of each species contributing to one mole of the overall glass formulation. For the glass with x = 0.05 we obtain, $[Na^+] + 2[Ca^{2+}]$ = 0.982 moles from its composition. From the ^{29}Si, ^{31}P and ^{11}B NMR spectra we find that $[Si^{(3)}] + 2\,[Si^{(2)}] + 3\,[P^{(0)}] + 2\,[P^{(1)}]$ = 0.832 moles, leading to the conclusion that $[B^{(2)}] + 2[B^{(1)}]$ = 0.15 moles. Thus, the 0.1 mole of boron possess an average anionic charge of 1.5. Considering the fact that the four-coordinate boron atoms are likely to be mono-anionic, we conclude that the majority of the three-coordinate boron species must be di-anionic, corresponding to pyroborate groups.

While, in principle, the same kind of data analysis can be attempted for the sample containing 1% B_2O_3 the relative error caused by the experimental uncertainties of the silicate and phosphate speciations will be five times as large, and hence, the conclusions will be less reliable.

Another question of interest concerns the connectivity of the borate species, i.e. the extent to which they are linked to other network forming structural units. Considering previous findings in alkali modified bioactive (silica-free) borophosphate glasses, which suggest the preferred formation of B-O-P linkages [32], the question arises if such linkages can also be detected in the present (silica-dominated) glass system. As described in the literature, the rotational echo double resonance (REDOR) method is well-suited to address this question, as it recouples the heteronuclear ^{11}B-^{31}P dipole-dipole interaction via coherent inversion pulse trains applied during a desired number of rotor periods [26,27,33]. Figure 6 and Table 5 summarize the results obtained on these glasses and further of model compound BPO_4, used for calibration purposes based on the second moment calculated from its internuclear distances [34]. The extremely low $M_{2(B\text{-}P)}$ values measured in these glasses indicate that the number of B-O-P linkages in which both the three- and the four-coordinated boron species are involved are negligible. We can thus conclude that in these glasses no preferential boron-phosphorus interactions are discernible. This result is noteworthy with regard to previous $^{31}P/^{11}B$ heteronuclear correlation (HETCOR) spectra of glasses with similar compositions, which revealed clearly detectable heteronuclear magnetic dipole-dipole coupling between these two nuclear species [13] in boron-containing bioglasses with similar compositions. As pointed out by these authors, these HETCOR-crosspeaks cannot arise from direct B-O-P linkages, but instead must be attributed to dipolar couplings at more remote

distances. From two-spin model calculations, we may conclude from the curvature of the data shown in Figure 6, that the minimum B-P distances in our glasses are near 5.0 Å.

Reference 13 further presents data from ^{11}B single quantum/double quantum correlation spectroscopy, suggesting strong homonuclear ^{11}B-^{11}B dipole-dipole couplings indicating the presence of $B^{(4)}$-O-$B^{(4)}$, $B^{(4)}$-O-$B^{(2)}$, and $B^{(2)}$-O-$B^{(2)}$ linkages in glasses containing as little as 5 mole% B_2O_3. In the present study, we have tested this prediction by homonuclear spin echo decay spectroscopy [25]. This method has been previously proven to give reliable quantitative information about homonuclear dipole-dipole interactions in quadrupolar spin-3/2 systems if the central transition is selectively excited [25]. In the present case, these conditions are fulfilled for the three-coordinated boron species, which constitute the majority of the boron inventory. The results of this analysis are shown in Figure 7 and summarized in Table 5. Using the measurement data on glassy B_2O_3 for calibration, and assuming the same three B-O-B distances as in the $B^{(3)}$-unit of crystalline B_2O_3 (248.8, 248.9, and 249.7 pm) [35], we may conclude from the spin echo decay data of the two boron-containing glasses that there is at least one B-O-B linkage per boron. This result is nicely consistent with our conclusion that the predominant three-coordinate boron species is a pyroborate ($B^{(1)}$) unit.

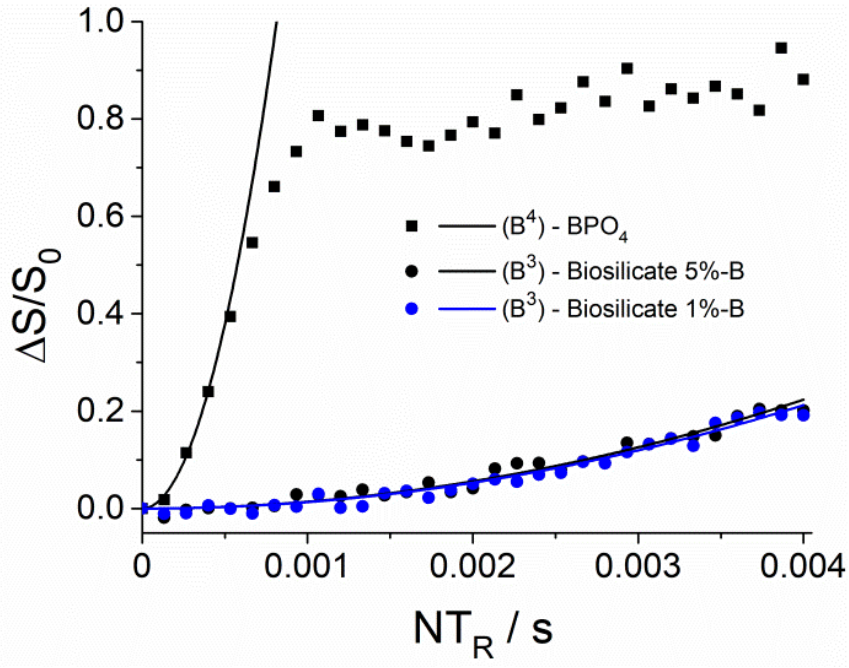

Figure 6: $^{11}B\{^{31}P\}$ REDOR data measured on Biosilicate precursor glasses, containing 1 and 5 mole % B_2O_3 and of the crystalline BPO_4 model compound.

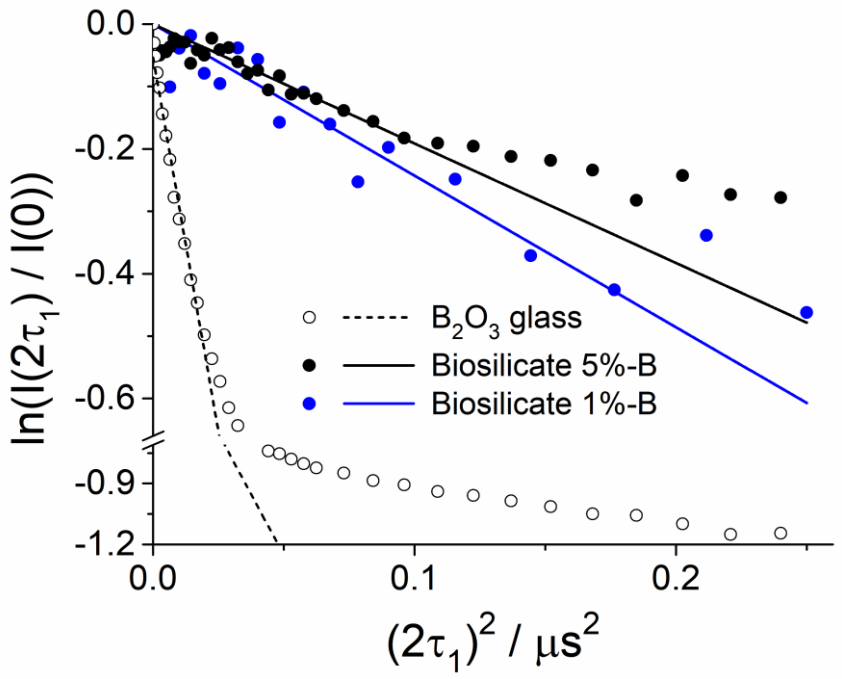

Figure 7: ^{11}B spin echo decays measured on the two bioactive glasses and of glassy B_2O_3 serving as a model material.

Table 5: Homo- and heteronuclear dipolar second moments M_2 of samples and model compounds, obtained from REDOR and spin echo decay experiments characterizing the mean ^{11}B-^{11}B and ^{11}B-^{31}P dipolar coupling strengths. Values in parentheses reflect the corresponding internuclear ^{11}B-^{11}B distance assuming a two-spin system. The quality facor *f* states the agreement of theoretical and practical second moment of the reference substance BPO4 with which the sample's experimental second moments have been corrected.

Sample	Species	$M_{2(B\text{-}P)}$ / 10^6 rad^{2}s^{-2} ± 10%	$M_{2(B\text{-}B)}$ / 10^6 rad^{2}s^{-2} ± 10%
BPO_4	Exp. Theo.[a]	11.2 19.1 (f = 0.59)	-
B_2O_3 glass	Exp. Theo.[b]	-	47.95 97.04
1% B_2O_3	B^{III} B^{IV}	0.17 0.07 (data not shown)	4.86 (3.1 Å)
5% B_2O_3	B^{III} B^{IV}	0.17 0.06 (data not shown)	3.83 (3.3 Å)

[a]Calculated from powder diffraction data [30]
[b]Calculated from powder diffraction data of the isochemical crystal [31]

Structural characterization of the crystallized samples

Figure 8 shows the X-ray powder diffraction results obtained upon crystallization of the precursor glasses. All three samples show the reflections of the principal crystalline phase, $Na_2CaSi_2O_6$. The sample with x = 0.05 shows additional reflections near 23°, 32°, and 47°, which could not be attributed to a specific phase. The presence of $NaCaPO_4$, easily detected by ^{31}P MAS-NMR (see below), could not be identified in the XRD powder pattern.

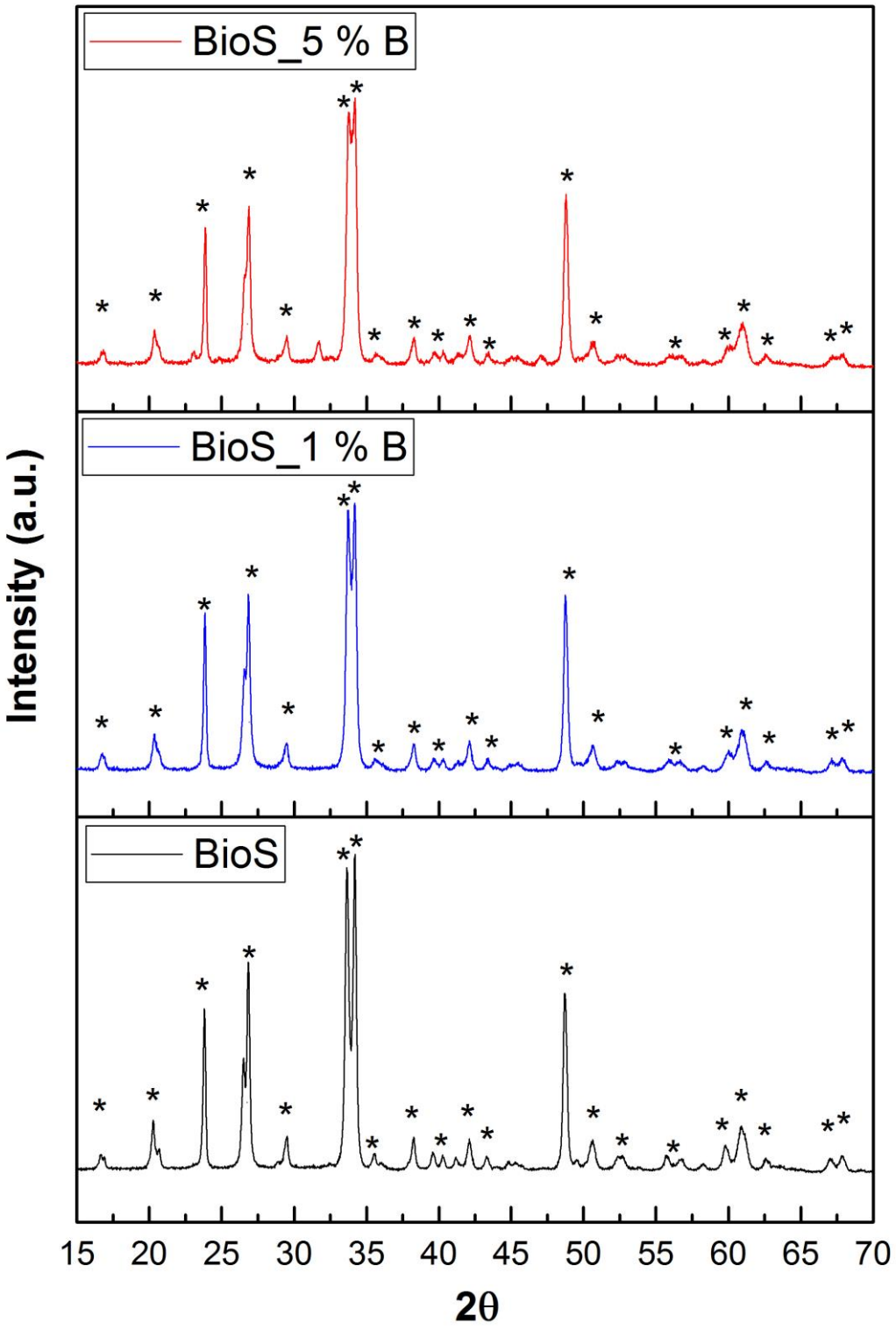

Figure 8: X-ray powder diffractograms of the Biosilicate precursor glass samples after heat treatment for crystallization. Asterisks denote the reflections due to $Na_2CaSi_2O_6$.

Figures 9-12 summarize the MAS-NMR spectra of ^{29}Si, ^{31}P, ^{11}B, and ^{23}Na of the crystallized samples, including their lineshape simulations. Crystallization of the precursor glasses results in pronounced spectroscopic changes. The ^{29}Si MAS-NMR spectra of the three crystallized specimens are identical within experimental error, showing only one Gaussian component at δ = -89.5 ± 0.5 ppm, *FWHM* = 5.4 ± 0.1 ppm, which identifies the crystalline sodium calcium silicate compound $Na_2CaSi_2O_6$, compare also Table 6. The relatively large linewidth signifies considerable disorder, presumably caused by the random distribution of the two counterions Na^+ and Ca^{2+} in the compound's lattice. The ^{31}P MAS-NMR spectrum of the crystallized boron-free sample (Figure 10) shows that only minor amounts of P species are crystallized, yielding a sharp signal near 3.0 ± 0.2 ppm, suggesting the formation of $NaCaPO_4$ previously identified as an intermediate crystallization stage of apatite-leucite glass-ceramic precursors [36]. Moreover, we can identify three broad resonances near -22, -4, and +11 ppm, which can be assigned to $P^{(2)}$, $P^{(1)}$, and $P^{(0)}$ units, respectively. All of these peaks show some structure, indicating a deviation from a plain Gaussian distribution. This structure may arise from different local phosphate configurations characterized by different numbers of Na^+ and Ca^{2+} ions for charge compensation. To account for this lineshape, each of the $P^{(n)}$ components was simulated by two Gaussian peaks about 4-5 ppm apart from each other. The fitting model is shown in Figure 10 for the central peaks only; however, the area analysis listed in Table 7 also includes the results obtained from fitting the first two sets of spinning sidebands as well. To explore connectivity of these phosphate species with boron, the sample containing 5% boron oxide was subjected to a $^{31}P\{^{11}B\}$ REAPDOR experiment. As indicated in Figure 11, the near-absence of a dipolar recoupling effect gives no evidence for B-O-P connectivity in the residual glassy material. This result indicates that the residual glass material formed upon crystallization of the sodium-calcium silicate should not be viewed as a borophosphate glass. Evidently, the thermal treatment conditions applied for nucleation and growth did not result in a formation of a homogeneous glassy phase, for which a substantial REAPDOR effect would have been expected. [32,33]

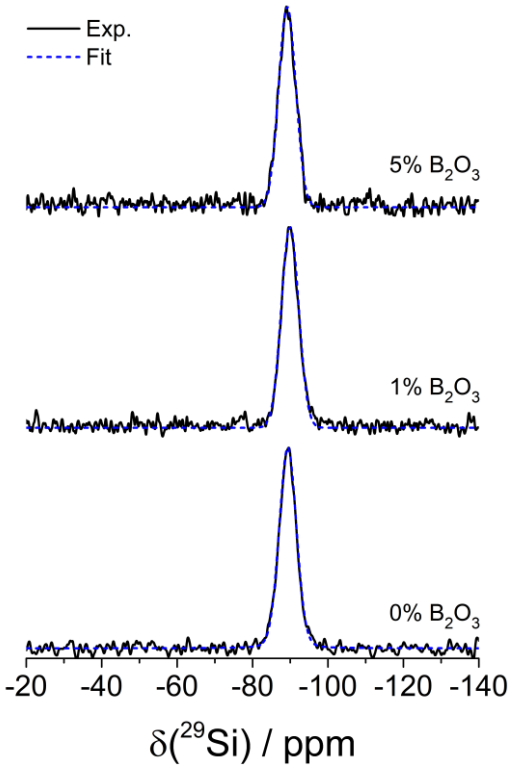

Figure 9: ^{29}Si MAS-NMR spectra of the samples after heat treatment for crystallization.

Table 6: ^{29}Si MAS-NMR parameters measured for biosilicates.

x	δ_{iso} / ppm ± 0.5 ppm	FWHM / ppm ± 0.5 ppm	*F* / % ± 1%
0.00	-89.4	5.4	100
0.01	-90.0	5.4	100
0.05	-89.2	5.4	100

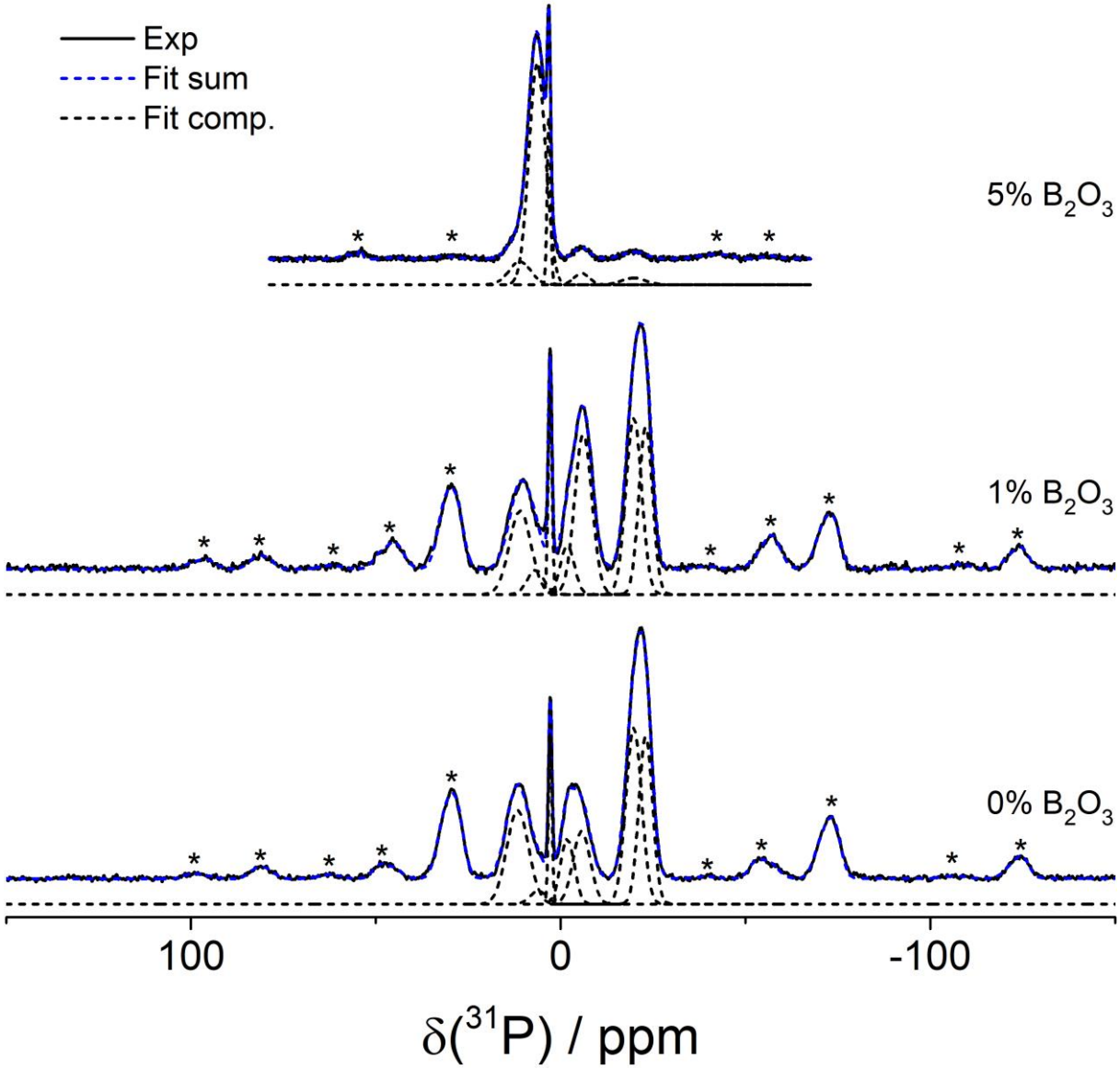

Figure 10: ^{31}P MAS-NMR spectra of the biosilicate precursor glass samples after heat treatment for crystallization. Spinning sidebands are indicated by asterisks. Dashed curves indicate the simulation model for the central MAS bands, based on the parameters listed in Table 7. The quantitative proportions listed there include corresponding simulations of the MAS sidebands as well.

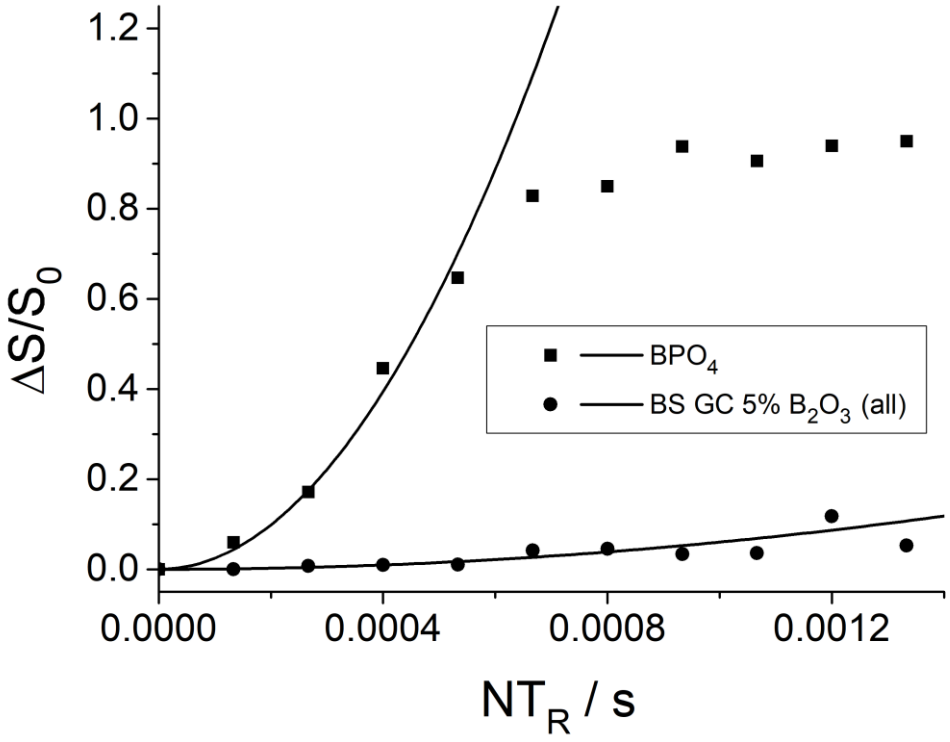

Figure 11: $^{31}P\{^{11}B\}$ REAPDOR curve of BPO_4 and of partially crystallized biosilicate glass containing 5% B_2O_3, indicating the absence of B-O-P connectivity in the latter.

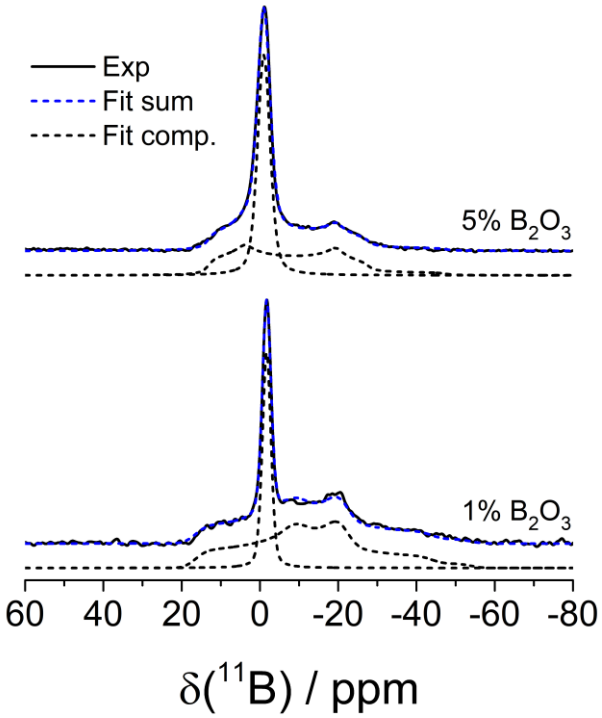

Figure 12: ^{11}B MAS-NMR spectra of the biosilicate precursor glass samples after heat treatment for crystallization. Dashed curves show simulated lineshape components.

Table 7: Isotropic chemical shifts, linewidths and fractional areas (including spinning sidebands) of the ^{31}P MAS-NMR spectral components of boron-containing biosilicate glass ceramic after crystallization.

x	Species	δ_{iso} / ppm ± 0.5 ppm	FWHM / ppm ± 0.5 ppm	*F* / % ± 2%
0.00	$P^{(0)}$ glass-	11.6	6.9	15
	$P^{(0)}$ glass	6.0	5.3	2
	$NaCaPO_4$	2.8	1.1	4
	$P^{(1)}_{0B}$ glass	-1.8	4.4	9
	$P^{(1)}_{0B}$ glass	-5.7	5.5	12
	$P^{(2)}_{0B}$ glass	-19.8	5.0	31
	$P^{(2)}_{0B}$ glass	-23.0	4.3	27
0.01	$P^{(0)}$ glass	11.0	6.8	12
	$P^{(0)}$ glass	6.8	5.3	2
	$NaCaPO_4$	2.9	1.2	5
	$P^{(1)}_{0B}$ glass	-1.8	4.4	6
	$P^{(1)}_{0B}$ glass	-6.1	5.5	24
	$P^{(2)}_{0B}$ glass	-19.8	5.0	28
	$P^{(2)}_{0B}$ glass	-23.0	4.3	23
0.05	$P^{(0)}$ glass	11.0	6.9	11
	$P^{(0)}$ glass	6.3	5.3	70
	$NaCaPO_4$	3.2	1.0	11
	$P^{(1)}_{0B}$ glass	-5.7	4.9	4
	$P^{(2)}_{0B}$ glass	-19.8	7.3	4

Table 8: ^{11}B MAS-NMR spectral fitting parameters of the glass-ceramics under study.

		B^{III}				B^{IV}		
X	B_0 / T	δ_{iso} / ppm ± 0.5 ppm	CQ / MHz ± 0.1 MHz	η_Q	*F* / % ± 1%	δ_{iso} / ppm ± 0.5 ppm	FWHM / ppm ± 0.5 ppm	*F* / % ± 1%
0.01	5.7	17.6	2.5	0.67	84	-1.7	2.6	16
0.05	5.7	18.4	2.5	0.25	49	-1.0	3.8	51

The ^{11}B MAS-NMR spectra (Figure 12) also show profound changes after thermal treatment. In both samples, the fractions of four-coordinated boron are greatly increased relative to that in the glassy precursors supporting the formation of a mixed sodium calcium borate glassy phase. The ^{11}B chemical shifts, see Table 8, differ significantly from those in borophosphate glasses [32,33], thus offering no evidence for B-O-P linkages. For the $x = 0.05$ sample there is a significant ^{11}B MAS-NMR lineshape change for the three-coordinate boron species. Lineshape analysis indicates a much smaller electrostatic field gradient asymmetry parameter η_Q than before crystallization. These observations suggest that following the crystallization of the sodium-calcium silicate, the pyroborate unit actually breaks down, and is being converted into uncharged three-coordinate boron species as well as singly-charged $B^{(4)}$ units. This

pronounced change is a consequence of the Na^+ and Ca^{2+} depletion in the residual glassy phase once the crystalline sodium calcium silicate phase has precipitated out. In contrast, for the $x = 0.01$ sample, the residual glassy phase may still contain some pyroborate, even though the amount of four-coordinate boron is also increased significantly. Unfortunately these structural interpretations cannot be tested by spin echo decay spectroscopy as the $B^{(4)}$ species does not fulfill the spin-dynamics criteria for a valid decay analysis (no sufficiently selective excitation of the central transition achievable) [25].

Finally, Figure 13 compares the ^{23}Na MAS-NMR spectra for the three samples before and after crystallization. In the glassy materials, the typical asymmetric peak pattern is observed, which is characteristic of an electric field gradient distribution caused by the distribution of local environments in the glassy state. After crystallization, a relatively sharp peak is observed near 15 ppm, which we attribute to crystallized $NaCaPO_4$. The dominant broader component must arise from crystallized $Na_2CaSi_2O_6$. Although the peak shape is narrower than in the original glass, the asymmetric peak shape still reflects a great deal of structural disorder, which we can attribute to the variation of local environments that is caused by the statistical distribution of Ca^{2+} and Na^+ ions over the cationic sublattice sites [37]. For both the glassy and the crystalline samples, the effect of disorder was modeled via a Czjzek distribution [38], implemented within the DMFIT program [24], yielding the lineshape parameters summarized in Table 9.

Table 9: ^{23}Na MAS-NMR spectral fitting parameters of the glass-ceramics under study.

X		**δ_{iso} / ppm ± 0.5 ppm**	**C_Q / MHz ± 0.1 MHz**	**F / % ± 1%**
0	Glass	6.2	3.0	100
	Glass-ceramic	15.0	1.1	13
		0.9	2.5	87
0.01	Glass	6.5	3.2	100
	Glass-ceramic	15.1	1.1	11
		2.5	2.5	89
0.05	Glass	10.6	2.7	100
	Glass-ceramic	15.0	1.0	14
		0.9	2.3	86

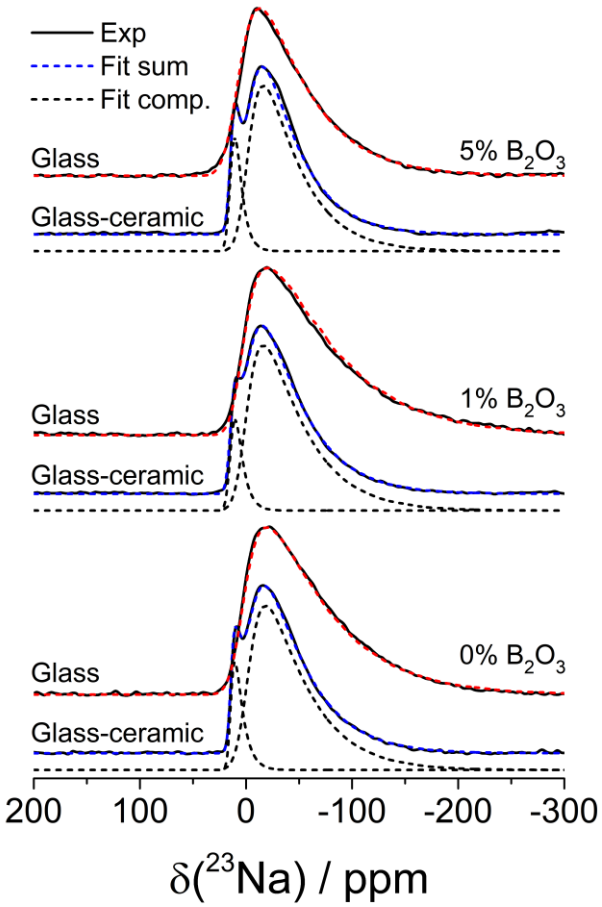

Figure 13: ^{23}Na MAS-NMR spectra of the biosilicate precursor glass samples after heat treatment for crystallization. Dashed curves show simulated lineshape components based on the Czjzek model of a distribution of local electric field gradients [38].

Conclusions

In summary, we have conducted a detailed study of boron incorporation into biosilicate before and after crystallization. For this particular glass, somewhat surprisingly, boron increases the glass transition temperature and reduces the crystallization stability. It has only a weak influence upon the dissolution kinetics in TRIS-buffer solution.

The influence of silicate for borate substitution on the structural organization of Biosilicate precursor glass was investigated by multinuclear solid-state single and double resonance NMR spectroscopy. Solid state ^{11}B NMR indicates that boron is likely present in the form of three-coordinate pyroborate units, with only minor fractions of four-coordinate species present. In contrast, ^{31}P MAS-NMR spectra revealed that phosphorus is almost exclusively present in the form of orthophosphate. The demand of the anionic borate network former for cationic charge compensation leads to an increase in the average connectivity of the silicate network, as evident from ^{29}Si NMR. ^{31}P/^{11}B dipolar recoupling experiments indicate that borate–phosphate linkages can be neglected in these glasses, presumably because of the low

borate and phosphate concentrations. Crystallization of the glassy biosilicate precursor produced crystalline $NaCaPO_4$ and $Na_2CaSi_2O_6$ as well as a residual amorphous material, for which also no B-O-P linkages could be detected. The latter result indicates that under the heat treatment conditions applied, no melt equilibration of the residual glassy material towards the formation of a borophosphate glass has taken place

Acknowledgements

The authors would like to acknowledge the Brazilian funding agencies São Paulo Research Foundation FAPESP (CEPID Project 2013/07793-6) and CNPq. H.B. also thanks for support from the Deutsche Forschungsgemeinschaft.

References

[1] M.C. Crovace, M. T. Souza, C. R. Chinaglia, O. Peitl Filho, E.D. Zanotto, *J. Non-Cryst. Solids*, 432 (2016), 90-110.

[2] C. I. A. van Houdt, C.R. Tim, M. C. Crovace, E.D.Zanotto, O. Peitl Filho, D. J. O.Ulrich, J. A. Jansen, N. A. Parizotto, A. C. Renno, J. J. J. P van den Beucken, Biomed. Mater.10 (2015) 035003.

[3] E. P. Ferraz, F. S. Oliveira, P. T. Oliveira, M. C. Crovace, O. Peitl Filho, M. M. Beloti, A. L. Rosa, J. Biomed. Mater. Res. A, 105 (2017), 419-423.

[4] P. Balasubramanian, T. Buettner, P.V. Miguez, A.R. Boccaccini, J. Eur. Ceram. Soc. 38 (2018), 855-869.

[5] C. Wu, J. Chang, J. Controlled Release 193 (2014**),** 282-295.

[6] P. Rico, A. Rodrigo-Navarro, M. Salmerón-Sánchez Tissue Engineering A 21 (2015) 2662-2672.

[7] O. Sych, O. Gunduz, N. Pinchuk, G.E. Stan, F. N. Oktar, J. Austral. Ceram. Soc. 52 (2016) 103-110.

[8] H. B. Pan, X. L. Zhao, X. Zhang, K.B. Zhang, L.C. Li, W. Li, M. Lam, W.W. Lu, D.P. Wang, W.H. Huang, K.L. Lin, J. Chang, J. R. Soc. Interface 7 (2010) 1025-31.

[9] C.Wu, R. Miron, A. Sculean, S. Kaskel, T. Doert, R. Schulze, Y. Zhang,. Biomaterials 32 (2011) 7068-78.

[10] C. Wu, J. Chang, J. Controlled Release 193 (2014) 282-295.

[11] Q. Yang, S. Chen, H. Shi, H. Xiao, Y. Ma, Mater. Sci. Engin. C 55 (2015) 105-107.

[12] Y. Yu, M Eden, RSC Adv. 6 (2016), 101288-101303.

[13] Y. Yu, B. Stevensson, M. Eden, M., J. Phys. Chem. B 121(2017), 9737-9752.

[14] N. Sharmin, M.B. Hasan, C. D. Rudd, D. Boyd, U. Werner-Zwanziger, I. Ahmed, A. J. Parsons, J. Biomed. Mater. Res. 105B (2017), 764-777.

[15] M. Eden, P. Sundberg, C. Stalhandske,. J Non-Cryst. Solids 357 (2011), 1587-1594.

[16] D. Carta, J C. Knowles, P. Guerry, M. E. Smith, R. J. Newport, J. Mater. Chem. 19 (2009), 150-158.

[17] K. McDonald, M. A. Hanson, D. Boyd, J Non-Cryst. Solids 443 (2016), 184-191.

[18] K. O'Connell, M. Hanson, H. O'Shea, D. Boyd, J Non-Cryst. Solids 430 (2015), 1-8.

[19] F. R. V. Turcu, A. Samoson, M. Maier, D. L. Trandafir, S. Simon, J. Am. Ceram. Soc. 99 (2016), 2795-2800.

[20]O. Peitl, E. D. Zanotto, F.C. Serbena, L.L. Hench, Acta Biomaterialia 8, (2012), 321-332.

[21] E.D. Zanotto, C. Ravagnani, O. Peitl, H. Panzeri, L. E. H. Guimarães. Patent WO2004074199A1, 2004.

[22] ISO 23317:2012. Implants for surgery -- In vitro evaluation for apatite-forming ability of implant materials. 2012.

[23] ISO 10993-14:2001. Biological evaluation of medical devices -- Part 14: Identification and quantification of degradation products from ceramics. 2001.

[24] D. Massiot, F. Fayon, M. Carpon, L. King, S. Le Calvé, B. Alonso, J.-O. Durand, B. Bujoli, Z. Gan, G. Hoatson, Magn. Reson. Chem. 40 (2002), 70-76.

[25] B. Gee, H. Eckert, Solid State Nucl. Magn. Reson 5 (1995), 113-121.

[26] T. Gullion, Magn. Reson. Rev. 17 (1997), 83-131.

[27] T. Gullion, J. Schaefer, J. Magn. Reson 81(1989), 196-200.

[28] J. H. Van Vleck, Phys. Rev. 74 (1948), 1168-1183.

[29] M. Bertmer, H. Eckert, Solid State Nucl. Magn. Reson. 15 (1999), 139-152.

[30] T. Gullion, Chem. Phys. Lett. 246 (1995), 325-330.

[31] H. Eckert, Prog. Nucl. Magn. Reson. Spectrosc. 24 (1992) 159-293 and references therein.

[32] D. Zielniok, C. Cramer, H. Eckert, Chem. Mater. 19 (2007), 3162-3170.

[33] D. Larink, H. Eckert, M. Reichert, S. W. Martin, J. Phys. Chem. C. 126 (2012), 26162-26176.

[34] J. Haines, C. Chateau, R. Astier, P. Fertey, O. Cambon, Z. Kristallogr. 219, (2004), 32-37.

[35] B. T. Gorres, P.W. Montgomery, C. D. Knutson, G. E. Gurr, Acta Crystallogr. B 26, (1970), 906-915.

[36] J. C. C. Chan, R. Ohnsorge, K. Meise-Gresch, H. Eckert, W. Höland, Chem. Mater. 13 (2001) 4198-4206.

[37] H. Ohsato, I Maki, Y. Takeuchi, Acta Crystallogr. C 41 (1985), 1575-1577.

[38] J.B. D'Espinose de Lacaillerie, C. Freitigny, D. Massiot, J. Magn. Reson. 192 (2008), 244-251.